© 2014. Published by The Company of Biologists Ltd | The Journal of Experimental Biology (2014) 217, 3870-3882 doi:10.1242/jeb.102202

RESEARCH ARTICLE

Chevron formation of the zebrafish muscle segments

Fabian Rost[1], Christina Eugster[2], Christian Schröter[2,*], Andrew C. Oates[2,3,4] and Lutz Brusch[1,§]

ABSTRACT

The muscle segments of fish have a folded shape, termed a chevron, which is thought to be optimal for the undulating body movements of swimming. However, the mechanism shaping the chevron during embryogenesis is not understood. Here, we used time-lapse microscopy of developing zebrafish embryos spanning the entire somitogenesis period to quantify the dynamics of chevron shape development. By comparing such time courses with the start of movements in wildtype zebrafish and analysing immobile mutants, we show that the previously implicated body movements do not play a role in chevron formation. Further, the monotonic increase of chevron angle along the anteroposterior axis revealed by our data constrains or rules out possible contributions by previously proposed mechanisms. In particular, we found that muscle pioneers are not required for chevron formation. We put forward a tension-and-resistance mechanism involving interactions between intra-segmental tension and segment boundaries. To evaluate this mechanism, we derived and analysed a mechanical model of a chain of contractile and resisting elements. The predictions of this model were verified by comparison with experimental data. Altogether, our results support the notion that a simple physical mechanism suffices to self-organize the observed spatiotemporal pattern in chevron formation.

KEY WORDS: Biomechanical model, Development, Morphogenesis, Myotome, Quantitative analysis, Teleost

INTRODUCTION

All chordates have metameric muscle segments that are critical for locomotion. These muscles are termed myotomes, and their characteristic shape in aquatic species (Fig. 1) is referred to as a chevron (Hoar et al., 1969; Kimmel et al., 1995). Typically, one observes three folds in sagittal sections of adult fish like salmon and zebrafish (Agassiz and Vogt, 1845; Greene and Greene, 1913; Maurer, 1913; Videler, 1993), but there can be up to six (Harder, 1964). The oldest known fossils with chevrons are *Pikaia* (Morris and Caron, 2012) and *Haikouichthys* (Shu et al., 1996). They are present in amphioxus (Bone and Moore, 2008; Hatschek, 1882; Hatschek, 1893; Nursall, 1956), the most basal extant chordate (Delsuc et al., 2006), the agnathan lamprey (Langelaan, 1904; Nursall, 1956; Wickström, 1897), the tadpole of the anuran *Xenopus* (Harrison, 1898; von Seckendorff Hoff and Wassersug, 1986) and in salamander larvae (Bordzilovskaya et al., 1989; Francis, 1934; Gegenbaur, 1859; Mchedlishvili et al., 2007).

[1]Center for Information Services and High-Performance Computing, Technische Universität Dresden, 01062 Dresden, Germany. [2]Max Planck Institute of Molecular Cell Biology and Genetics, 01307 Dresden, Germany. [3]MRC-National Institute for Medical Research, The Ridgeway, Mill Hill, London NW7 1AA, UK. [4]Department of Cell and Developmental Biology, University College London, Gower Street, London WC1E 6BT, UK.
*Present address: University of Cambridge, Department of Genetics, Downing Street, Cambridge CB2 3EH, UK.

[§]Author for correspondence (lutz.brusch@tu-dresden.de)

Received 29 January 2014; Accepted 4 September 2014

The myotome's locomotory function has been conserved for at least 500 million years (Bone and Moore, 2008), suggesting that the chevron shape has been optimized for this function (Hoar et al., 1969; Videler, 1993). Chevron shape and function are currently used to infer evolutionary relationships among chordates (Lacalli, 2012; Mallatt and Holland, 2013; Morris and Caron, 2012). Although the mechanics of chevron-shaped myotomes during swimming has been studied for over a century (Alexander, 1969; Chevrel, 1913; Nursall, 1956; Rauther, 1940; van der Stelt, 1968; van Leeuwen, 1999; van Leeuwen et al., 2008; Videler, 1993; Willemse, 1966; Wunder, 1936), the development of the chevron remains poorly understood.

How does the chevron pattern emerge during embryogenesis? We addressed this question in the zebrafish *Danio rerio* (Hamilton 1822). Its embryo facilitates investigation of morphological changes, notably somitogenesis (Durbin et al., 2000; Henry et al., 2005; Holley et al., 2000; Schröter et al., 2008; Schröter et al., 2012; van Eeden et al., 1996), myotome differentiation (Cortés et al., 2003; Currie and Ingham, 1996; Daggett et al., 2007; Devoto et al., 1996; Henry and Amacher, 2004; van Raamsdonk et al., 1974a; van Raamsdonk et al., 1978; Yin and Solnica-Krezel, 2007) and chevron formation (van Raamsdonk et al., 1974a; van Raamsdonk et al., 1974b; van Raamsdonk et al., 1977; van Raamsdonk et al., 1979). As early development progresses, somites sequentially bud off the unstructured paraxial mesoderm (Fig. 1A–C; supplementary material Movies 1, 2) and commit most of their cells to myotome formation, thereby respecting and further enforcing tissue segmentation (Kimmel et al., 1995; Morin-Kensicki et al., 2002). We will use the terms segment and segment boundary for both somites and myotomes and their boundaries, respectively.

About 35 segments form within ~15 h (Schröter et al., 2008). Initially, segments appear as cuboidal blocks (Fig. 1A). The anteriormost segments retain their cuboidal shape; more posterior segments deform into V-shaped chevrons with the apex pointing anteriorly (van Eeden et al., 1996; van Raamsdonk et al., 1974a). However, reports differ as to the timing of chevron formation (starting when seven or 12 segments have formed) (van Eeden et al., 1996; van Raamsdonk et al., 1974a). van Raamsdonk et al. (van Raamsdonk et al., 1974a) reported that segments five to 12 deform simultaneously. Tail segments (18–35) start to deform immediately after each somite has formed (van Raamsdonk et al., 1974a). The timing and the extent of shape changes of segments 13–17 have not been reported. Three weeks after hatching, W-shaped myotomes emerge (van Raamsdonk et al., 1974a). Together, these findings indicate temporal and spatial heterogeneities but their quantification is incomplete. Pioneering quantitative work measured the chevron angles of the anal segment for different time points (van Raamsdonk et al., 1979), but earlier and more frequent measurements are required to constrain mechanistic models. In this study, our first goal was to provide a definitive description of chevron formation using quantification of time-lapse microscopy of the developing zebrafish embryo.

The processes driving chevron formation during embryogenesis and larval stages were first investigated in the 1970s by van Raamsdonk et al. (van Raamsdonk et al., 1974a; van Raamsdonk et

The Journal of Experimental Biology

The Journal of Experimental Biology (2014) doi:10.1242/jeb.102202

List of symbols and abbreviations

a	distance between apex of chevron and the initially straight border (Fig. 2B)
E	energy in the mechanical model
F_x	forces exerted by the springs in the segments of the mechanical model
h	dorsoventral height of a segment
hpf	hours post-fertilization
i	segment index; counted from anterior to posterior
K	dimensionless model parameter indicating the stiffness of the boundary relative to the stiffness of the intra-segment springs
K_x	spring constant of springs within a segment of the mechanical model
K_α	resistance of the segment boundaries of the mechanical model against bending
L	anteroposterior length of a segment
L_0	rest length of springs within a segment of the mechanical model
n	number of segments in the mechanical model
N	number of individuals
nc	notochord
t	time; the average time point of the formation of segment 1 is t=0 if not stated otherwise
t_{start}, t_{end}	fit parameters describing the time points at which chevron formation started and ended
x_i	anteroposterior extension of the spring in segment i of the mechanical model
α	chevron angle between the dorsal segment boundary and the dorsoventral axis, calculated from measurement of γ_{min}, γ_{max}
α_{end}	fit parameter describing the final chevron angle
$\alpha_i(t)$	chevron angle of segment i of the mechanical model at time t
α_{min}, α_{max}	minimum and maximum angle α, calculated from γ_{max} and γ_{min}, respectively
γ	measured angle between the dorsal extremity of the posterior segment boundary and the dorsal roof of the notochord
γ_{min}, γ_{max}	minimum and maximum angle of γ (Fig. 2A)
Δα	uncertainty of measurement of α
$\Delta\alpha_{end}$, Δt_{start}, Δt_{end}	errors of the fit parameters

al., 1974b; van Raamsdonk et al., 1977; van Raamsdonk et al., 1979). Below, we introduce four competing hypotheses seeking to explain chevron formation, namely body movements, templating of the chevron from the posterior border of the head, relative tissue movements, or differential growth or tonic muscle tension associated with muscle pioneer cells.

First, given the accepted importance of the chevron shape for locomotion, the undulating lateral movements that herald the onset of locomotion were suggested to play a role in the morphogenesis of the chevron (te Kronnié, 2000; van Raamsdonk et al., 1974a; van Raamsdonk et al., 1977; van Raamsdonk et al., 1979). When testing this hypothesis by immobilizing young fish with developed chevrons, a slight straightening of the chevron angles was observed. The fish recovered the normal pattern when it could move again. Independently, and arguing against a strong role for swimming movements in chevron development, the genetically immobile homozygous *nic*^{b107} mutant zebrafish forms chevrons (Schröter et al., 2008; van der Meulen et al., 2005). However, this formation has never been quantified. Thus, a contribution from movement to the dynamics of chevron formation, or the final angle of the chevron, may yet be present.

Second, independent of motion, a templating hypothesis for chevron formation posits that the posterior border of the head already possesses the chevron shape, and this pattern can be passed to the next segment. Muscle cells may simply grow to a predefined size, so that when the muscle cells connect to the next segment's anterior boundary, this segment would also form a chevron (van Raamsdonk et al., 1979). Unless interrupted, this pattern would be passed sequentially into the tail. Inconsistent with templating as the sole determinant, chevrons develop immediately posterior to segments with experimentally disrupted shapes (Riedel-Kruse et al., 2007; Windner et al., 2012). However, a contribution to the final shape by templating is not ruled out.

The third hypothesis features relative movement of structures in the embryo (Turner, 2007). The myosepts were proposed to attach to the notochord to be pulled into chevron shape. This hypothesis can be tested by time-lapse microscopy.

Finally, tonic muscle contraction and differential growth within the myotome have also been considered as potential mechanisms (van Raamsdonk et al., 1979). The earliest developing muscle fibres, the muscle pioneers, elongate in concert with the formation of chevrons (Kimmel et al., 1995). Mutants that fail to differentiate muscle pioneers do not have normal V-shaped chevrons when examined at larval stages, instead displaying a U-shaped chevron (Halpern et al., 1993; te Kronnié, 2000; van Eeden et al., 1996). It is thus now widely believed that the muscle pioneers and/or the myoseptum are responsible for the chevron shape (Dolez et al., 2011; Koumans and Akster, 1995; Meyers et al., 2013), but this has not been directly tested, and a mechanism whereby these cells would cause the chevron shape has not been proposed.

In summary, these four hypotheses represent a range of mechanisms that are not mutually exclusive, but for which there is currently no conclusive experimental support. Our second goal was to test these hypotheses by comparing their predictions with our quantitative data.

Independent of which, if any, of the proposed mechanisms will be confirmed, it is clear that morphogenesis of the chevron is ultimately executed by mechanical forces. These might act (1) autonomously in each segment in a segment-specific and genetically encoded manner. Alternatively, by analogy to chevron patterns in abiotic systems such as rock formations in geology (Bayly, 1974) and polymers and liquid crystals in material science (Read et al., 1999; Singer, 1993), the chevron might emerge (2) collectively as a result of force fields across the tissue with initially homogeneous properties and without the need to invoke genetically encoded and segment-specific properties. Our third goal was to test whether the latter scenario is possible by formulating a mechanical model, motivated by correlations revealed by our quantitative data analysis.

In this study, we quantified time-lapse light microscopy movies of chevron formation for mobile, immobile and muscle pioneer-ablated zebrafish embryos. Analysis of these data disproves three of the four previously hypothesized mechanisms and restricts any potential role for muscle pioneers to chevron maintenance. We then propose a tension-and-resistance mechanism for which chevrons form collectively and formalize it in a mechanical model that shows qualitative agreement with our data. We suggest further tests and extensions of our model and briefly discuss our results in the light of evolution.

RESULTS

Measurement of chevron formation in zebrafish embryos

We quantified chevron formation using time-lapse imaging of embryos from in-crosses of free-spawning heterozygous *nic*^{b107} parents (Herrgen et al., 2009; Schröter et al., 2008). Wild-type and heterozygous *nic*^{b107} mutant zebrafish show undulatory swimming

The Journal of Experimental Biology (2014) doi:10.1242/jeb.102202

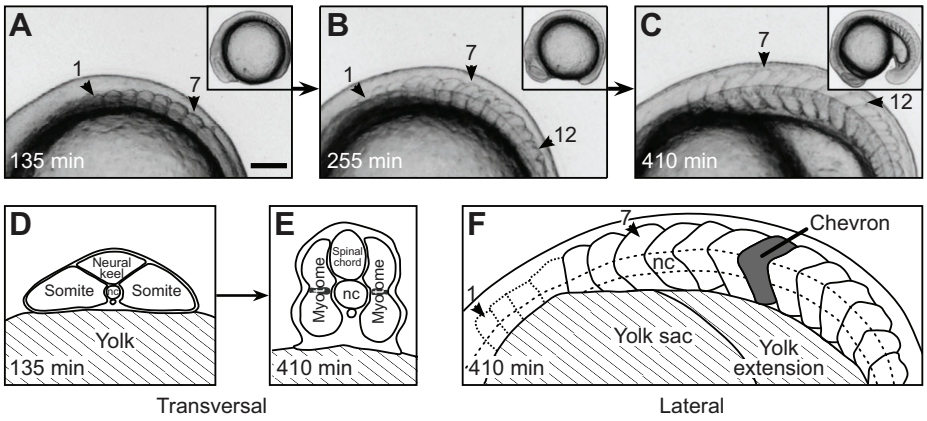

Fig. 1. Trunk and segment morphology of a developing zebrafish embryo. (A–C) Lateral views of a developing zebrafish embryo from a representative time-lapse movie (supplementary material Movie 1). Anterior is to the left. Arrowheads mark segments 1, 7 and 12. Insets show the entire embryo. Scale bar, 100 µm. (A) Seven cuboidal segments have formed. (B) Twelve segments have formed. Segment 1 is cuboidal, segment 7 already has a chevron shape, the most recently formed segment 12 still is cuboidal. (C) Eighteen segments have formed. Segment 12 now is chevron shaped. (D,E) Illustrations of transversal sections of the anterior trunk at the level of segment 7. [Copyright 2000 Wiley. Modified and used with permission from Stickney et al. (Stickney et al., 2000).] (D) At the time of somite formation (segment 7 as representative), the trunk is initially flattened and mediolaterally extended, with the notochord (nc) in the middle. (E) Later, when the segment has completed the rapid morphogenesis of the chevron, the trunk is dorsoventrally extended. The shaded regions in the middle of the segment indicate the position of the muscle pioneers. (F) Sketch of C. Visible segment boundaries are shown as solid lines and the poorly visible boundaries of the first four segments as dotted lines. One chevron-shaped segment is marked in grey. The notochord (dashed line) intersects the apexes of the chevrons.

movements (supplementary material Movie 1), whereas the homozygous *nic*^{b107} mutant remains still throughout the observation period (supplementary material Movie 2). We will refer to homozygous *nic*^{b107} mutant embryos as ‘immobile’, and both wild-type and heterozygous *nic*^{b107} embryos as ‘mobile’. We analysed time-lapse microscopy movies of three mobile and five immobile zebrafish from the beginning of segmentation until the end of chevron formation. The time point of the formation of segment 1 was chosen as t=0. Below, we first focus on mobile embryos.

We oriented the embryos laterally, affording a view of the segmenting paraxial mesoderm in which the forming straight somite boundaries could be seen reliably (Fig. 1A). As the somites matured into myotomes and changed their shape from a cuboidal block to a chevron, we could observe the deformation of segments (Fig. 1B,C). Through this 16 h time window, the overall shape of the embryonic axis deformed as the segmenting mesoderm converged from a flattened mediolaterally extended cross-section (Fig. 1D) to a dorsoventrally extended cross-section (Fig. 1E). In each time-lapse frame, the medially located notochord was visible as a reference line that intersected with the apex of the forming chevron (Fig. 1F).

To quantify the emergence of the chevron shape, we measured the angle $\gamma=(\gamma_{max}-\gamma_{min})/2$ between the dorsal extremity of the posterior segment boundary and the dorsal roof of the notochord in each time-lapse movie frame (Fig. 2A; supplementary material Table S1 and Fig. S1). Next, we transformed the measurements of γ_{min} and γ_{max} to $\alpha=90\ \text{deg}-(\gamma_{max}+\gamma_{min})/2$, the angle between the dorsal segment boundary and the dorsoventral axis (Fig. 2B). The error is given by $\Delta\alpha=(\gamma_{max}-\gamma_{min})/2$. We show these data for segment 1, 7 and 15 from a representative embryo in Fig. 2C–E. Because of the high contrast of the yolk edge, the anterior-most segments were difficult to follow, leading to gaps in the time series (Fig. 2C). In contrast, more posterior segments yielded near-continuous time series of chevron angle values until the start of occasional movements at 7.3±0.2 h also introduced intermittent gaps (grey regions in Fig. 2C–E; supplementary material Movie 1).

The anterior-most segment (segment 1) did not form a chevron (Fig. 2C). Strikingly, the chevron angle of segments 6 and 15 changed smoothly over a time interval of about 2 h before reaching the final chevron shape, which remained constant until the end of the recording (Fig. 2D,E).

Based on the data for each single segment, we identified non-chevron-forming segments as those for which most of the measured angles α were close to 0 deg. For them, we calculated the final angle α_{end} as the mean of all measured angles (Fig. 2C, orange). To capture the dynamic behaviour of each chevron-forming segment in a compact and informative manner, we described the change in the chevron angle over time with three parameters: α_{end}, the final chevron angle, where $\alpha_{end}=0$ deg means no chevron formation and a typical posterior chevron has $\alpha_{end}\approx40$ deg; and the time points at which chevron formation started (t_{start}) and ended (t_{end}). These parameter values were determined for each segment by fitting a piecewise linear function to the time series (Fig. 2D,E). We restricted our analysis to trunk segments 1 to 15, as the values for α_{end} did not change appreciably in segments 16–30 when compared with segments 8–15.

Quantitative description of chevron formation

For all quantified time series of mobile and immobile zebrafish, we first assessed which segments along the axis showed robust chevron formation. For segments 1 and 2, we did not observe embryos with significantly chevron-forming boundaries, regardless of mobility (Table 1). For both mobile and immobile embryos, segment boundaries deformed significantly at segments 4–15 (Table 1). We conclude that the two anterior segments do not form chevrons and that the transition from block-like to chevron-shaped myotomes occurs at segment number 3.

For segments 4–15, 96% of the datasets were of sufficiently high quality that the result of the curve fitting was accepted and these values are plotted in Fig. 3. For mobile embryos (green symbols), the deformation of boundaries of segments 4–7 starts nearly simultaneously, whereas the boundary deformation of segments 8–15 starts sequentially and with a small offset after the formation of the segment boundary (Fig. 3A, green symbols). Boundary deformation of all quantified segments in mobile embryos ceased

The Journal of Experimental Biology (2014) doi:10.1242/jeb.102202

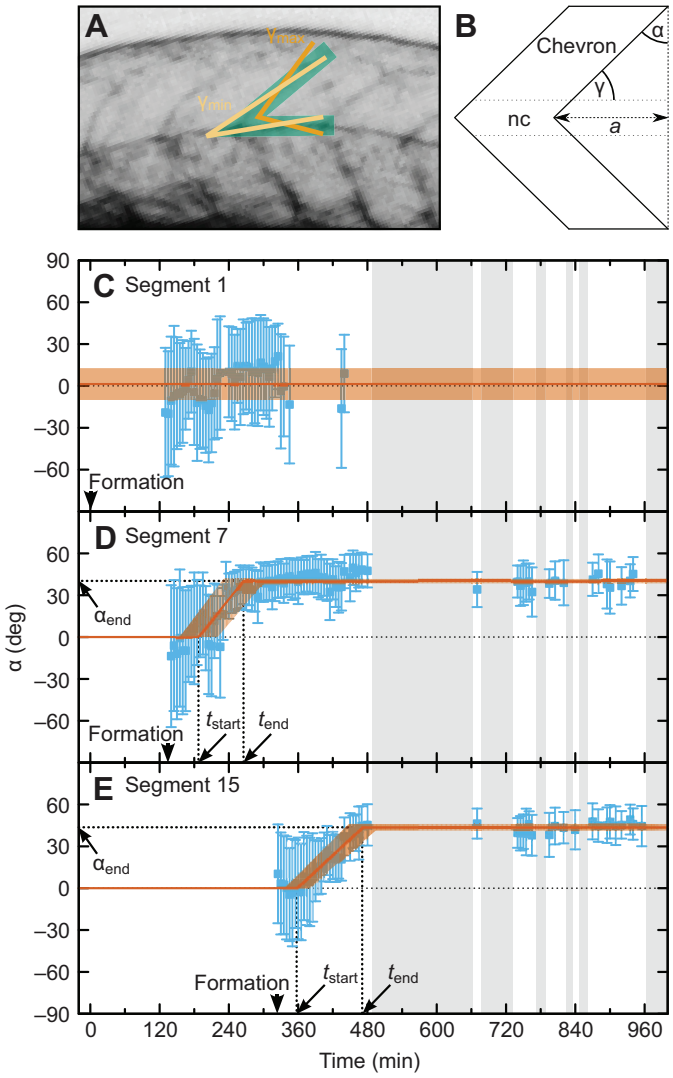

Fig. 2. Quantification of changing chevron angles for representative anterior and posterior segments. (A) Measurement of the chevron angle. The green area marks the posterior segment boundary and the dorsal notochord boundary in the maximum projection from a *z*-stack. The light and dark orange lines mark the measured angles γ_{min} and γ_{max}, respectively. (B) Sketch of a bent segment boundary showing the geometrical relationship between γ and chevron angle α. Measured angles γ_{min} and γ_{max} were transformed into $\alpha\pm\Delta\alpha$ [$\alpha=90\ \text{deg}-(\gamma_{max}+\gamma_{min})/2$, $\Delta\alpha=(\gamma_{max}-\gamma_{min})/2$; see Materials and methods]. For straight boundaries, α is 0; α>0 indicates a bent boundary; *a* is the distance between the apex of the chevron and the initially straight border. (C–E) Blue: angle measurements for segments 1 (C), 7 (D) and 15 (E) of the embryo shown in Fig. 1 as a function of time. The error bar shows the 68% confidence interval. The thin dotted black line shows α=0, meaning no chevron. Grey shaded intervals indicate lack of data due to autonomous movements of the animal. (C) Segment boundary 1 stays straight (on average α=1±11 deg, shown in orange). (D,E) Segment boundaries 7 and 15 form a chevron. Arrowheads mark segment formation time. The fit with a piecewise linear (described by the three parameters chevron formation start time t_{start}, end time t_{end} and final chevron angle α_{end}, indicated by thick dotted lines) is shown in orange with the uncertainty of the fit depicted by the transparent orange area. (D) t_{start}=187±33 min, t_{end}=265±34 min, α_{end}=40±2 deg. (E) t_{start}=357±21 min, t_{end}=471±24 min, α_{end}=44±2 deg.

2±1 h after the start of chevron formation (Fig. 3A,B, green symbols). The data for the final chevron angle group the segments in a similar way as the chevron formation start time: whereas the final chevron angle monotonically increases for segments 1–7, the more posterior segments homogeneously acquire 40±3 deg (Fig. 3C, green symbols).

Complementing previous studies of chevron shape in later developmental stages with established chevrons (van der Meulen et al., 2005; van Raamsdonk et al., 1974a; van Raamsdonk et al., 1977; van Raamsdonk et al., 1979), the results here represent the first quantitative measurements of the dynamics of chevron formation in any species. Thus, the first goal of this study has been reached and we can now compare our data with the predictions of hypothetical mechanisms for chevron formation.

Body movements

To test whether the normal undulating body movements resulting from rhythmic muscle contraction have an influence on early chevron formation, as has previously been proposed (van Raamsdonk et al., 1974a; van Raamsdonk et al., 1977; van Raamsdonk et al., 1979), we used our data to quantitatively relate the dynamics of chevron formation and the start of movements. As expected (van Raamsdonk et al., 1974a), we found that movements start after the anterior segments 4–17 have already started to deform (Fig. 3A; supplementary material Movie 1). Hence, movements are not required for chevron formation to start. Segments 4–13 had already finished chevron formation before movements started in wild-type embryos.

To what extent movements contribute to chevron formation dynamics and to setting the final chevron angle can also be determined by comparison with non-moving embryos. The *nic*^{b107} mutant is ideally suited for this purpose as it has a lesion in the nicotinic cholinergic receptor that prevents neurotransmitter from motor neurons from activating muscle contraction, consequently paralysing the embryo (Sepich et al., 1994; Sepich et al., 1998; Westerfield et al., 1990). The data for immobile *nic*^{b107} homozygous embryos confirm that chevrons form (Fig. 3, orange symbols), as expected (Schröter et al., 2008; van der Meulen et al., 2005). As then expected for segments 4–13, which ceased chevron formation before the start of movements in mobile embryos, mobile and immobile embryos showed very similar timing of chevron formation, t_{start} and t_{end}.

Importantly, no significant difference was found between mobile and immobile embryos in the values of final chevron angle α_{end}, based on 8 h of recording after movements of wild-type embryos had started. Strikingly, no significant differences were found for segments 14 and 15. We conclude that the movements of early rhythmic muscle contraction that precede swimming have no effect on the formation of chevrons in the zebrafish embryo.

Simple chevron templating

The data in Table 1 and Fig. 3C can also be used to test the previously proposed templating mechanism for chevron formation (van Raamsdonk et al., 1979). If the chevron shape is simply copied from a chevron-shaped surface at the back of the head, then we would expect the same chevron angle for all segments, but this was not observed at any stage of chevron formation. Thus, our new data do not support the idea that templating alone is responsible for the development of the chevron shape in the anterior trunk.

Inhibition of muscle pioneer differentiation

The data presented above rule out the body-movement, simple-templating and notochord-movement hypotheses (see Discussion). Muscle pioneer cells are thought to be responsible for chevron formation (Dolez et al., 2011; Meyers et al., 2013). Muscle pioneers

The Journal of Experimental Biology (2014) doi:10.1242/jeb.102202

Table 1. Percentage of embryos showing significant chevron formation

	Segment														
	1	2	3	4	5	6	7	8	9	10	11	12	13	14	15
Mobile (%)	0	0	0	100	100	100	–	100	100	–	100	100	100	–	100
Immobile (%)	0	0	–	80	100	100	100	100	100	100	100	100	100	100	100

Only segments for which the fitting gave significant results can be considered as significantly chevron-forming segments (green columns); for definition, see Materials and methods. Segments are marked if none of the quantified individuals could be identified as significantly chevron forming. An unambiguous classification of segment 3 requires more individuals and more time points to be quantified. Number of individuals *N* is 3–5. Dash indicates *N*<3, result not valid.

can be identified by *engrailed2* expression (Fig. 4A). Embryos treated with 0.2% DMSO carrier form normal chevrons, indistinguishable from wild-type embryos grown in E3 medium only, as illustrated by *cb1045* expression at segment boundaries (Fig. 4B). We blocked muscle pioneer differentiation by inhibiting Shh signalling with cyclopamine (Barresi et al., 2001; Wolff et al., 2003) (Fig. 4C). As expected, segment boundaries showed a U-shape phenotype at 36 hpf (hours post-fertilization) (Fig. 4D), resembling U-mutants. We performed time-lapse imaging of these muscle pioneer-ablated embryos as described above (Fig. 4E–H; supplementary material Movie 3). Segment formation progressed along the axis at the same rate as under normal conditions (data not shown). Although the chevron angle with cyclopamine treatment had a larger measurement error, surprisingly, we found that many chevrons formed with a normal angle at around 400–500 min (Fig. 4F,H; supplementary material Fig. S2). Subsequently, the chevron shape was not maintained (Fig. 4G,H; supplementary material Fig. S2) and relaxed into a U-shape (Fig. 4D). For the majority of the analysed segments, the wild-type start- and end-times of bending were in good agreement with the transient bending of muscle pioneer-ablated embryos (orange curve in Fig. 4H).

DISCUSSION

Insufficiencies of three proposed mechanisms to explain chevron formation

Our quantitative comparison of mobile and immobile embryos rules out a role for swimming motions of the embryo in both the timing and final shape of the embryonic chevrons, thereby corroborating and extending earlier evidence. This finding does not impact the acknowledged importance of the myotome's chevron shape for swimming mechanics.

We quantified final chevron angles as function of segment index and found a monotonic increase for segments 4–7 that also start formation simultaneously, whereas segments 1 and 2 do not form chevrons (Fig. 3). An earlier report described this transition between segments 4 and 5 (van Raamsdonk et al., 1974a), instead of segment 3, which may reflect the lower spatial and temporal resolution of earlier methods. However, van Raamsdonk et al. used a slightly lower temperature, which might shift the transition. Our data rule out the simple templating hypothesis according to which each angle is just a copy of its earlier formed anterior neighbour. This observation agrees with the results of Riedel-Kruse et al. (Riedel-Kruse et al., 2007) in which correct segmentation was transiently perturbed and then rescued. Although segments 7–17 did not form correctly and thereby would be unable to pass on a chevron pattern, the more posterior segments were shaped as chevrons again. Recently, Windner et al. (Windner et al., 2012) rescued defective somitogenesis in the *fss* mutant by transient expression of the Fss/Tbx6 protein. They observed one or two contiguous chevrons, where the tissue immediately anterior was not chevron shaped, again inconsistent with a simple templating mechanism for chevron formation. Nevertheless, the posterior boundary of any segment is the anterior boundary for the next segment and can thereby influence its shape.

The anchoring hypothesis of Turner (Turner, 2007) requires an anterior-ward movement of the notochord at the time of chevron formation. In contrast, our time-lapse movies showed a strong posterior-ward movement of the notochord relative to the segment boundaries (supplementary material Movie 2), but this was observable only after the vacuolating cells of the notochord became visible, which occurs after completion of chevron formation. Confocal time-lapse movies revealing the posterior-ward sliding of the notochord have been reported (Barrios et al., 2003), but these were recorded slightly before chevron formation of the corresponding segments. Thus, there is no continuous anterior-ward movement of the notochord that would be consistent with the anchoring hypothesis. It remains formally possible that a wavefront of transient reversal of the direction of notochord sliding propagates along the axis in concert

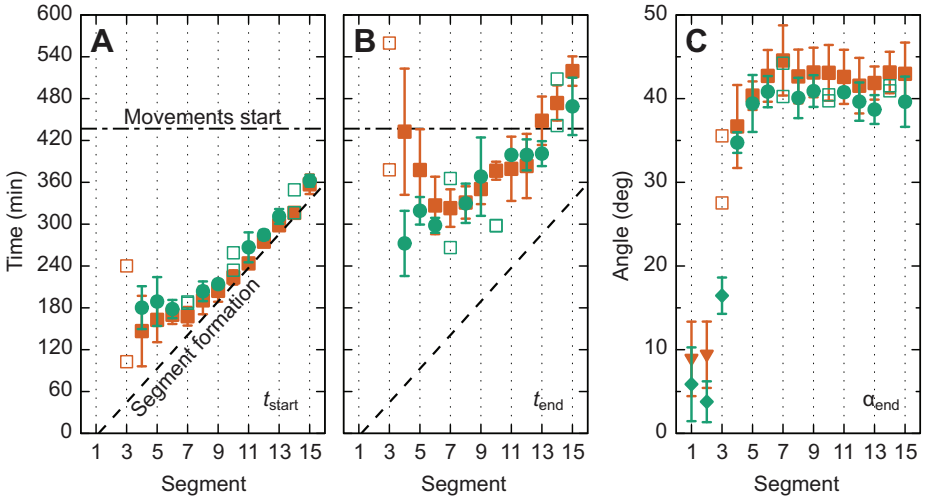

Fig. 3. Chevron formation for mobile and immobile embryos. (A–C) Filled symbols with error bars depict mean and standard deviation (number of animals *N*=3–5) for the fit parameters (A) chevron formation start time t_{start}, (B) end time t_{end} and (C) final chevron angle α_{end} as a function of segment index. In cases where *N*<3, single measurements are plotted as open symbols. Green circles, mobile embryos; orange squares, immobile embryos. (A,B) The solid black curve indicates somite formation times (Schröter et al., 2008). The horizontal long–short dashed line denotes the average onset of autonomous movements. (C) In addition to the fitting results, the mean angles for non-chevron-forming segments are shown as green diamonds and orange triangles for mobile and immobile embryos, respectively.

The Journal of Experimental Biology (2014) doi:10.1242/jeb.102202

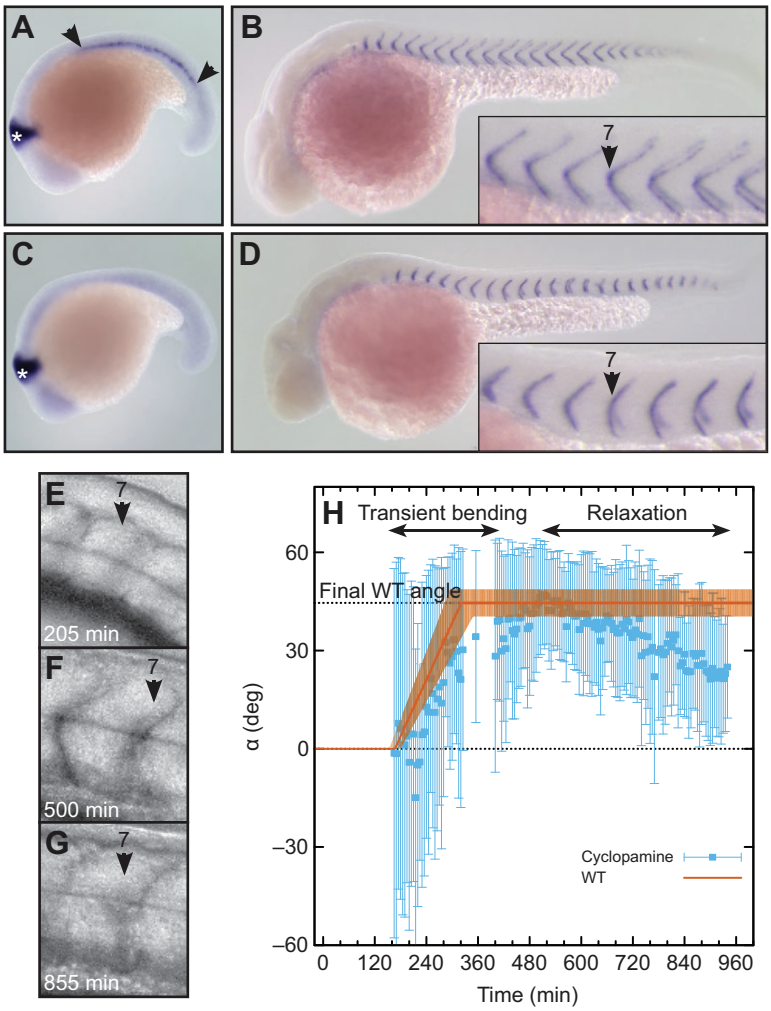

Fig. 4. Role of muscle pioneers in chevron maintenance, but not formation. (A,B) Embryos treated with 0.2% DMSO alone (control). (A) *engrailed2* (*en2*) *in situ* hybridization at 18 somite stage. Muscle pioneers are stained by *en2* (area between arrowheads). The midbrain is marked with a white asterisk. (B) *cb1045 in situ* hybridization at 36 hpf (hours post-fertilization) to visualize segment boundaries. (C,D) Embryos treated with 7.5 µmol l^{-1} cyclopamine from bud stage. (C) *en2 in situ* hybridization at 18 somite stage. Muscle pioneers are absent. (D) *cb1045 in situ* hybridization at 36 hpf. Boundaries are U-shaped. (E–G) Lateral views of segment 7 of an embryo treated with 7.5 µmol l^{-1} cyclopamine from bud stage. (E) Newly formed segment is cuboidal. (F) At 500 min, the segment has a clear chevron shape. (G) At 855 min, the chevron relaxed into a U-shape. (H) Quantification of chevron angles of the segment shown in E–G (blue squares and error bars). The orange line shows the typical bending of an immobile embryo (piecewise linear function with parameters for segment 7 from Fig. 3, uncertainty depicted by the transparent orange area). WT, wild-type.

with chevron formation. However unlikely this proposal seems, time-lapse microscopy targeted to the notochord at this time point would be required to resolve the question.

U-shaped myotome mutants and the role of muscle pioneers

Zebrafish mutants have been reported in which somites form normally but the myotomes display a U-shape instead of a chevron at larval stages. These phenotypes have been associated with the failure to form a specific cell type in the myotome, the muscle pioneer at the apex of the chevron. The first genetic evidence of a role for these cells in chevron patterning came from the *no tail* (*ntl*) mutant, encoding a zebrafish Brachyury/T transcription factor, in which muscle pioneers fail to form and myotomes take on a U-shape (Halpern et al., 1993). Most of this class of mutants encode components of the Sonic Hedgehog signalling pathway, which is required for the differentiation of the adaxial cells, a columnar epithelium that is apposed to the notochord (Hatta et al., 1991; Weinberg et al., 1996), into early muscle fibre types such as the muscle pioneer (Johnston et al., 2011; Stickney et al., 2000). In *kny;tri* double-mutants, adaxial cells do take on a muscle fibre fate, but do not show proper spanning of the segment. Even in this case the chevron shape gets weaker (Yin and Solnica-Krezel, 2007). However, the relationship between these cells and the development of the chevron has not been explored and the surgical removal of muscle pioneer precursor cells in a few segments did not result in obviously altered segment shapes (Honjo and Eisen, 2005). Similarly, the inhibition of muscle pioneers by Dorsalin-1 in two consecutive segments did not lead to altered chevrons (Du et al., 1997).

Our own cyclopamine-treated embryos closely recapitulate the appearance of the original U-mutants; they lack muscle pioneers in early segmentation stages and they exhibit U-shaped myotomes at larval stages. However, the surprising observation of transient chevron shapes that mimic the normal untreated embryo with respect to maximum chevron angle as well as bending start- and end-time speaks against a role for muscle pioneers in chevron formation. High-level Shh signalling induces further cell types of the sclerotome (Fan and Tessier-Lavigne, 1994; Hammerschmidt et al., 1996), the dermomyotome (Feng et al., 2006), the spinal cord and other embryonic tissues. Our cyclopamine treatment likely also affected these Shh-dependent cell types and, hence, a requirement for any of them in chevron formation is also unlikely. Conversely, the observed failure to maintain the chevron shape may be due to the perturbation of any of the Shh-dependent cell types, including muscle pioneers. Our findings suggest that U-class mutants may similarly exhibit a failure of chevron maintenance, not formation. A potential role for other cell types in chevron formation remains to be investigated.

A mechanical model for the self-organization of heterogeneous chevron angles

The final angle of the chevron in subsequent segments increases monotonically in the anteroposterior direction until it reaches the maximum value of 40±3 deg at segment 7, which was also reached

The Journal of Experimental Biology (2014) doi:10.1242/jeb.102202

by all posterior segments that we analysed. Why is there such a strong segment dependence of chevron angle across the anterior segments? Is this because there is a molecular or genetic heterogeneity along the axis? Is it necessary that the pattern is pre-programmed so that each segment's angle is individually specified by genetic means, perhaps through a Hox gene code mechanism (Prince et al., 1998), or could the collective behaviour of segments with homogeneous properties self-organize the observed heterogeneous angles?

To investigate the latter possibility, we propose a mechanical model that is motivated by a series of published observations about the timing of cell differentiation and its coincidence with the timing of chevron formation, as reported here. The expression of the muscle-specific markers Eng protein and *myod* mRNA starts simultaneously in the anterior up to seven segments in the adaxial cells. For the more posterior segments, the two genes are expressed sequentially (Hatta et al., 1991; Weinberg et al., 1996). The muscle pioneers differentiate from the adaxial cells and later give rise to the myoseptum (Daggett et al., 2007; Devoto et al., 1996; Johnston et al., 2011). The cellular shape changes and cell migration that accompany the differentiation of other muscle types also start close to the notochord and simultaneously in the first five segments (Cortés et al., 2003; Daggett et al., 2007; Stickney et al., 2000; van Eeden et al., 1996; Yin and Solnica-Krezel, 2007) but then proceed posteriorly with constant time lag after segment formation (Henry and Amacher, 2004). In summary, these observations group the segments in the same way as our data analysis does: a group of anterior segments behaves differently from the complementary posterior segments (Fig. 5).

Although there are currently no measurements of the forces involved, it is plausible that the reported cellular rearrangements accompanying muscle differentiation generate tension from within the segments. Those cellular rearrangements start medially close to the notochord and the tension would act only medially on the segment boundaries and thereby bend them. Reinforced by the extracellular matrix, these boundaries will resist bending to some degree. The emergent behaviour induced by the tension cannot be foreseen intuitively as all segments are coupled and interact simultaneously. It

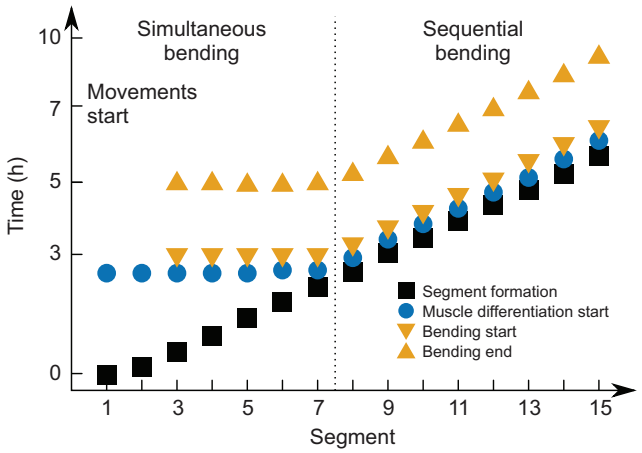

Fig. 5. Summary of chevron dynamics. Time of somite formation, approximate start of muscle differentiation (including cellular rearrangements and shape changes), and chevron formation start and end time are sketched as a function of segment index. Segments 1–7 differentiate simultaneously, i.e. anterior-most segments delay differentiation by up to 3 h after segmentation. Chevron formation of segments 1 and 2 is not detectable. Segments 4–7 deform simultaneously. Segments posterior to segment 7 differentiate and deform sequentially. For any segment, chevron formation takes 2 h from onset until the final angle is reached.

is possible to imagine all but the first segment acquiring equal shapes or, alternatively, multiple solutions may coexist and a fluctuation of a single initial segment shape could set up a pattern of mirrored chevrons to either side of the initial fluctuation.

The mathematical formalization of the model is required to understand whether the system is capable of showing the emergence of the experimentally observed heterogeneous pattern (Fig. 6). Note that this model assumes that tension is generated within the segment, but it is independent of how this tension is generated and it does not attempt an explicit description of individual cellular behaviours. Our model includes the case that the reported cellular rearrangements cause tension but it also encompasses other potential causes of tension. We reduce the model to two dimensions thanks to translational symmetry in the mediolateral direction. It consists of n=7 segments. Each segment has the same anteroposterior length L and dorsoventral height h but a variable chevron angle $\alpha_i(t)$ of its posterior boundary. The angle of the segment's anterior boundary is given as the angle $\alpha_{i-1}(t)$ of the posterior boundary of the corresponding neighbouring segment. We treat the anterior-most boundary between the head and segment 1 as stiff and straight, i.e. with a constant chevron angle of 0 deg. All segment boundaries are initialized as straight (Fig. 6A′). We then add harmonic springs (spring constant K_x, rest length $L_0<L$) in each segment that model the intra-segmental tension (Fig. 6B′). These springs contribute part of the energy of the model (see equation in Fig. 6D, blue). The resistance of the boundaries against bending is modelled by adding an energy penalty (strength K_α; see equation Fig. 6D, orange). Of course, the extension of the springs, x_i, and the chevron angles, α_i, are constrained by the geometry of the system (Fig. 6C′). Assuming $2L\approx h$ (true for zebrafish segments) and small α_i, we express this relationship in the formula for x_i (Fig. 6D, see Appendix).

With the derived energy and the initial conditions for α_i and the head boundary condition, we can calculate the final chevron angles in the steady state of the model and simulate the dynamics. We derive the steady state of our model by minimizing the energy (detailed calculations are in the Appendix). The relevant parameters are $K=K_\alpha/(K_xL^2)$, indicating the stiffness of the boundary relative to the stiffness of the intra-segment springs and L_0/L, the rest length of the spring in the segment relative to the segment length. We find that only one unique steady state exists. Independent of the chosen parameters and the number of segments, this state possesses monotonically increasing final chevron angles. The increase in chevron angle along the anteroposterior axis in the steady state is a robust property of the model (Fig. 6E). Importantly, the heterogeneous steady-state pattern does not need to be pre-determined by a complicated initial state but is found to self-organize from a completely homogeneous initial state (Fig. 6B′).

The model predicts that all segments would remain straight in the case of no intra-segmental contraction (L_0/L=1) or nearly straight (chevron angle below 1 deg) for very stiff boundaries (K>60) (see Appendix). For stiff segment boundaries (K>>1), the monotonic angle dependency can be approximated as an exponential function of segment index (see Appendix). Because an exponential function starts to increase slowly, the most anterior segments appear to remain straight.

To investigate the temporal dynamics of the model, we derive the over-damped equations of motion for the chevron angles from the system's energy (see Appendix). These equations can be solved numerically. The simulations show that a simultaneous onset of chevron formation is possible (Fig. 6F). This result is compatible with the experimental data. The particular shape of the time course depends on parameter values.

The Journal of Experimental Biology (2014) doi:10.1242/jeb.102202

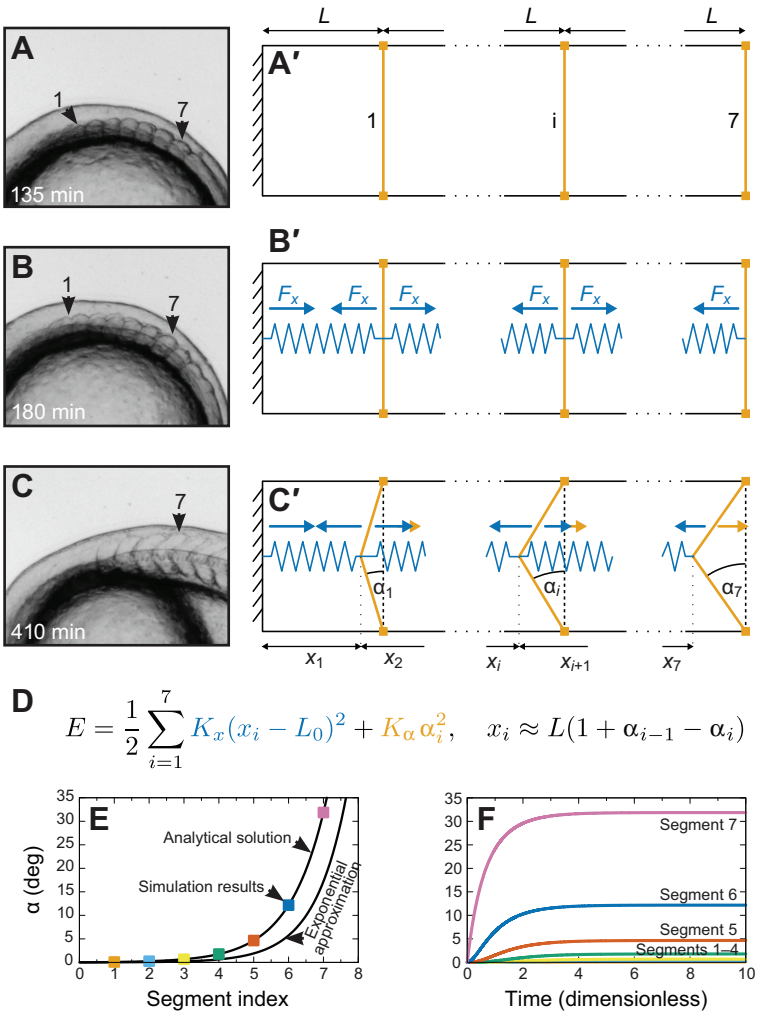

Fig. 6. A mechanical model for the establishment of chevron angles. (A–C) Representative segment shapes (see Fig. 1). (A) The first seven segments have formed with a cuboidal shape. (B) At about 180 min, chevron formation starts, hypothetically in accordance with the onset of muscle cell differentiation and concomitant rearrangements in the medial part of the segments that result in a contractile force. (C) At 410 min, segments 1–7 have their final shape. (A′–C′) Construction of a minimal mechanical model for chevron shape establishment. (A′) The model consists of seven segments. The most anterior segment (1), one intermediate segment (i) and the last segment (7) are sketched. The boundary anterior to segment 1 is the posterior boundary of the head and treated as stiff. We neglect the lateral dimension and assume that all segments have the same anteroposterior length L and dorsoventral height h. (B′) To model the hypothesized intra-segmental tension, we insert springs (blue) into each segment. The springs are identical (rest length L_0, spring constant K_x). Blue arrows depict the forces exerted on the segment boundaries. (C′) Except for the anterior boundary of segment 1, the segment boundaries are able to bend. The amount of bending is described by chevron angle α_i. We assume the dorsal and ventral tips of the boundaries (orange squares) to be fixed by the bulk segment tissue so that the segment length L cannot change and segment boundaries can only react to forces by bending. We assume the segment boundaries resist this bending, which results in forces in opposite direction (orange arrows). (D) This simple mechanical model is fully defined by specifying the energy E of the system. We choose the intra-segmental springs (blue in the equation) to be harmonic and add a penalty for bending of the segment boundaries to the energy (orange in the equation). This penalty depends harmonically on α_i and is of strength K_α. The second equation gives the constraints for x_i and α_i (see Appendix). (E) The final chevron angle in the steady state of our model as a function of segment index. Parameters are K=1, L_0=0.1 and seven segments. Black lines show the analytical solution and the exponential approximation as they are derived in the Appendix. The coloured squares are simulation results for the final angle from F. (F) Numerical solutions of the overdamped equations of motion (derived in the Appendix, parameters as before). For the chosen parameter values, the segments simultaneously start to form chevrons at t=0, the time the intrasegmental tension is switched on. Chevron angles increase monotonically for all segments. Segments reach their final chevron angle approximately at dimensionless time t=5. The most anterior segment boundaries 1–3 remain straight and therefore are hard to distinguish in the plot.

Taken together, we have reached our third goal: the observed spatiotemporal pattern of chevron angles could emerge from a homogeneous tissue without the need for additional genetic or biochemical differences between the segments.

Testing the mechanical model

Our mechanical model was motivated by stereotypical cellular rearrangements and differentiation of muscle fibres commencing around the time of chevron formation (Fig. 5). Importantly, the model is independent of which cellular or sub-cellular mechanisms might be at work. Direct tests of this hypothesis should seek to alter the generation or propagation of tension through the file of segments preceding the chevron transition. One possibility would be to ablate the first somite, thereby removing the fixed end of the chain, just before the onset of chevron formation at the seven somite stage. The proposed tension-and-resistance mechanism predicts that the angles of the forming chevrons will be altered: because segments will pull from both anterior and posterior sides, reversed chevron-shapes in

The Journal of Experimental Biology (2014) doi:10.1242/jeb.102202

the anterior and a central symmetrical segment are expected. From published material, a pattern with reversed chevrons was observed in frogs (Yoshigai et al., 2009). Another test might be to explant a row of somites from the embryo prior to the segment 7 transition, and ask whether a similar perturbation of chevron angles is observed as with the ablation of somite 1. If the somites could be separated from the file, or otherwise individually explanted (Beattie and Eisen, 1997; Laale, 1982), the autonomy of the chevron shape's development could be directly addressed. If somite 3 and somite 7, as examples, developed different chevron angles in isolation, our hypothesis of a collective mechanism would be contradicted.

If evidence supporting our general mechanical model was found, it would make sense to explore the cellular and molecular bases for this activity in some detail. Cellular candidates would include the rearrangement of the adaxial cells from epithelium to mesenchyme, or the development and migration of various muscle fibre types. Molecular candidates would include various force-generating systems such as cortical actin–myosin contractility, microtubule-associated processes or ion flux-regulated cellular volume changes.

Limits and extensions of the model

Our quantitative data analysis revealed a correlation between the reported onset of muscle differentiation and chevron formation. Our mechanical model of chevron formation provides an explanation of the position-dependent final chevron angles for the anterior segments. We note that we were not able to obtain a quantitative fitting to the final angle of these segments. We would have been able to fit the data by introducing a non-linear saturation term in the model, but in the absence of a specific biological motivation for this term we have avoided the unnecessary complication. Furthermore, segments 8–32 do not deform more than segment 7 and also appear sequentially, but both of these properties are currently ignored by our simple model. To account for the constant posterior segment boundary angles, we propose a model extension with time-dependent parameters that reflect the developmental maturation of muscle differentiation.

The measurements and model were made in 2D, yet the body is 3D. A potential role for tensions in the third dimension is worth considering if such tension becomes quantitatively measurable. For future studies, it will be important to quantify changes of body cross-section, cell rearrangements, muscle fibre elongation, and muscle fibre force as function of segment index and time, and to correlate these new data sets to our space–time plot of chevron formation (Fig. 5). Any observed correlations should then facilitate the identification of the mechanistic cause of the effective force field we have modelled here. Extensions into 3D are required to address the later changes towards the concentric series of cones in the adult (Greene and Greene, 1913; Shann, 1914; Videler, 1993).

Chevron patterns in other species

Chevron patterns exist in other species, including other fish, frogs, salamanders, lampreys, *Amphioxus* and the pre-Cambrian fossil *Pikaia*. Key cellular events that inspired our tension-and-resistance model are conserved. For instance, in *Amphioxus*, the chevron pattern forms in concert with cell elongation and muscle differentiation is delayed for anterior segments (Hatschek, 1882; Hatschek, 1893; Kaestner, 1892). In agreement with our proposed collective mode of chevron formation, several species including the tadpole of the frog *Leptodactylus albilabris* (Dent, 1956), *Pikaia* (Morris and Caron, 2012) and hagfish (Müller, 1836) show anterior straight segments and bent posterior segments. While most authors only distinguish straight anterior versus bent posterior segments, those species might actually show a monotonic increase in chevron angle. For the tadpole of the frog *Xenopus*, published figures show monotonically increasing final chevron angles for at least 10 anterior segments (Gray et al., 2009; Lee et al., 2010). It will be interesting to quantify angle time courses in *Xenopus* and to compare these with the correspondingly parameterized model.

Evolutionary aspects

The chevron shape itself and the shape's function in locomotion have been used to infer the evolutionary relationships among chordates (Lacalli, 2012; Mallatt and Holland, 2013; Morris and Caron, 2012). However, the development of the chevron, especially the mechanism underlying it, was largely ignored. The discussion of existing hypotheses and our proposed mechanism, which was motivated by quantitative correlations in fish but might be conserved across a number of other species (see above), may add to the emerging picture of chordate evolution.

Conclusion

We have quantified the time course of early chevron formation in terms of chevron formation start time, end time and final chevron angle for segments 1–15 for mobile, immobile and cyclopamine-treated zebrafish. These data reject or heavily constrain the possible contribution of a number of hypotheses. We find that muscle pioneers are not required for chevron formation but they and/or other high-level Shh signal-dependent cell types may be involved in chevron maintenance. We proposed a tension-and-resistance mechanism based on interactions between intra-segmental cell rearrangements and segment boundaries that explains the early phase of chevron development. A simple mechanical model allowed us to verify that this mechanism could account for the observed spatiotemporal pattern. A strong aspect of our model is the minimal set of ingredients it depends on and its nevertheless robust prediction of the observable monotonic increase in final chevron angle along the anteroposterior axis. An appropriate temporal order of muscle cell differentiation (Fig. 5) with uniform properties for all segments appears sufficient for the chevron pattern and its spatial dependencies to self-organize according to physical laws. Hence, evolution of segment-specific properties such as the increasing chevron angles across the anterior segments would not be necessary.

MATERIALS AND METHODS

Time-lapse movies

We analysed time-lapse movies of chevron formation during zebrafish development at 28°C, which were acquired in our previous studies (Herrgen et al., 2009; Schröter et al., 2008) using embryos from in-crosses of free-spawning heterozygous *nic*^{b107} parents (Westerfield et al., 1990). Frame rate was every 5 min. The formation of segment 1 was not always clearly detectable in the time-lapse movies. Therefore, we chose to set the time of the clearly detectable formation of segment 6 to 115 min for each individual movie, such that the average time point of the formation of segment 1 is t=0 (supplementary material Movies 1, 2).

Cyclopamine treatment

Cyclopamine-KAAD (cat. no. 239804, Calbiochem) was diluted in E3 medium to 7.5 µmol l^{-1} from a stock solution of 5 mmol l^{-1} in 100% DMSO. Manually dechorionated wild-type embryos were soaked in E3 medium containing cyclopamine-KAAD from 80% epiboly or bud stage until processed for *in situ* hybridization or to record somite formation in long-term time-lapse movies at 28°C. Embryos treated with 0.2% DMSO were indistinguishable from wild-type embryos grown in E3 only.

In situ hybridization

Embryos were fixed for 2 h or overnight with 4% paraformaldehyde in PBS at the 18 somite stage or at 36 hpf and stored in methanol. Antisense probes were generated against *engrailed2* (gift from Michael Brand) and *cb1045* (Riedel-Kruse et al., 2007) and *in situ* hybridization using NBT/BCIP was performed as described before (Oates and Ho, 2002) except that probes were hybridized at 55 and 60°C, respectively.

Quantitative image analysis

We analysed time-lapse light microscopy movies in which the image stacks show the development of embryos from before the one-somite stage until about the 30-somite stage. The embryos are visible in lateral view (supplementary material Movies 1, 2).

To quantify the shape of the chevron, we manually measured the angle between the posterior dorsal segment boundary and the notochord, γ, for successive time points using the angle tool in the Fiji package (Schindelin et al., 2012) (Fig. 2A,B). Assuming a simplified geometrical relationship that neglects notochord curvature, we can calculate angle α for all measured angle γ, which will be used for curve fitting and comparison with our mechanical model (Fig. 2B):

$$\alpha = 90\ \text{deg} - \gamma\,. \tag{1}$$

We determined averages α_{mean} and standard deviations $\Delta\alpha$ for a small number of segments by repeated manual evaluation of γ. Low contrast frames and intermittent occurrence of U-shaped contours left some uncertainty in the measurements.

To decrease the number of measurements, we approximate the averages α_{mean} and standard deviations $\Delta\alpha$ through only measuring the two extreme angles γ_{min} and γ_{max} (Fig. 2A). We define:

$$\alpha = \frac{\alpha_{max} + \alpha_{min}}{2}\,, \tag{2}$$

where α_{max} and α_{min} are calculated from the angles γ_{min} and γ_{max}, respectively (Fig. 2A). For the tested segments, α approximates the average of repeated measurements, α_{mean}, well. To calculate the uncertainty, we assumed the probability distribution for picking the true value α_t to be a Gaussian distribution around α_{mean}. Repeated manual evaluation of the likely angle α from the same image fell within the interval (α_{min}, α_{max}) in more than 95% of cases. Therefore, following the three-sigma rule, the standard deviation of the Gaussian is given by:

$$\sigma = \frac{1}{2}\Delta\alpha = \frac{1}{2}\frac{\alpha_{max} - \alpha_{min}}{2}\,. \tag{3}$$

Curve fitting

We considered all segments for which more than 80% of the data points fulfilled $\alpha_{mean} - \Delta\alpha \leq 0$ as non-chevron-forming segments (Fig. 2C). For the remaining segments, we fitted the data for each chevron-forming segment with a piecewise linear function (Fig. 2D,E). Hence, we will describe the chevron formation of these segments with the three parameters of the piecewise linear function: chevron formation start and end times, t_{start} and t_{end}, respectively, and a final chevron angle α_{end} that is reached after chevron formation ceased. We determined the fit parameters and their uncertainty using the bootstrap method (Press, 1996). For each segment, we calculated random samples of α for each time point using the Gaussian distribution defined by α_{mean} and $\Delta\alpha$. We generated 100 random data sets from the measured data for each segment and fitted each data set with the piecewise linear function. Thus, for each of the three parameters, we get N realizations from which we can calculate the mean, t_{start}, t_{end}, α_{end}, and the standard deviation, Δt_{start}, Δt_{end}, $\Delta\alpha_{end}$.

Fitting was done with a grid search using each parameter triple generated from all possible combinations of:

$$t_{start} \in \left\{t_{min},\, t_{min} + 10\ \text{min}, \ldots, t_{max}\right\}, \tag{4}$$

$$t_{end} \in \left\{t_{min},\, t_{min} + 10\ \text{min}, \ldots, t_{max}\right\}, \tag{5}$$

$$\alpha_{end} \in \left\{-1.0\ \text{rad}, -0.95\ \text{rad}, \ldots, 1.4\ \text{rad}\right\} = \left\{-57\ \text{deg}, -54\ \text{deg}, \ldots, 80\ \text{deg}\right\}, \tag{6}$$

where t_{min} is the formation time of the current segment boundary and t_{max}=740 min. Then the parameter combination with the minimal sum of squared residuals was chosen.

We considered fitting results insignificant if parameter uncertainties were too high. The criteria we chose for significance are:

$$\Delta\alpha_{end} < 6\ \text{deg}\,, \tag{7}$$

$$\Delta t_{start} < 60\ \text{min}\,, \tag{8}$$

$$\Delta t_{end} < 120\ \text{min}\,. \tag{9}$$

Furthermore we also considered fits invalid if the end of chevron formation might not have been in the observed period:

$$t_{end} + 2\Delta t_{end} > t_{max}\,. \tag{10}$$

We considered only segments with significant fitting results as chevron-forming segments, whereas we ignored the results for other segments and treated them as missing data.

APPENDIX

Constraints for α_i and x_i

For our mechanical model, the spring extensions, x_i, and the segment chevron angles, α_i, are geometrically constrained (Fig. 6C′). We will now deduce the relationship (Fig. 6D). In our time-lapse movies we measured the anteroposterior segment length, L, and the dorsoventral height, h, for various segments. The measurements showed:

$$2L \approx h\,, \tag{A1}$$

with a deviation smaller than 30%. We introduce the 'boundary extension', a_i (Fig. 2B). Simple trigonometry leads to:

$$\tan\alpha_i = \frac{a_i}{\frac{h}{2}}\,. \tag{A2}$$

Assuming small a_i and making use of Eqn A1, we get:

$$\alpha_i \approx \tan\alpha_i \approx \frac{a_i}{L}\,. \tag{A3}$$

For the first segment, the segment length is simply the sum of spring extension x_1 and 'boundary extension' a_1:

$$L = x_1 + a_1\,. \tag{A4}$$

For each following segment, similar reasoning leads to:

$$L = x_i + a_i - a_{i-1}\,. \tag{A5}$$

Defining $a_0 \equiv 0$, we can summarize the last two equations:

$$L = x_i + a_i - a_{i-1},\ i = 1 \ldots n\,. \tag{A6}$$

Using Eqn A3, we can write this as:

$$x_i \approx L\left(1 + \alpha_{i-1} - \alpha_i\right),\ i = 1 \ldots n\,. \tag{A7}$$

Calculating the minimal energy configuration

We will minimize the energy function (Fig. 6D):

$$E_n = \frac{1}{2}\sum_{i=1}^{n}\left(K_x\left(x_i - L_0\right)^2 + K_\alpha\alpha_i^2\right), \tag{A8}$$

to find the equilibrium state. The second equation in Fig. 6D formalizes our assumption that all segments have the same fixed length:

$$x_i \approx L\left(1 + \alpha_{i-1} - \alpha_i\right),\ i = 1 \ldots n,\ \alpha_0 \equiv 0\,. \tag{A9}$$

We now introduce the dimensionless quantities:

$$\tilde{E}_n = \frac{E_n}{K_x L^2},\ \tilde{x}_i = \frac{x_i}{L},\ \tilde{K} = \frac{K_a}{K_x L^2},\ \tilde{L}_0 = \frac{L_0}{L}\,. \tag{A10}$$

With these, we can write Eqns A8 and A9 as:

$$\tilde{E}_n = \frac{1}{2}\sum_{i=1}^{n}\left((\tilde{x}_i - \tilde{L}_0)^2 + \tilde{K}\alpha_i^2\right), \quad \text{(A11)}$$

$$1 \approx \tilde{x}_i + \alpha_i - \alpha_{i-1},\ i = 1\ldots n. \quad \text{(A12)}$$

Substituting the $\tilde{x}_i$ in Eqn A11 with Eqn A12 we get:

$$\tilde{E}_n = \frac{1}{2}\sum_{i=1}^{n}\left((1 - \alpha_i + \alpha_{i-1} - \tilde{L}_0)^2 + \tilde{K}\alpha_i^2\right). \quad \text{(A13)}$$

We will leave out the tildes for better readability from now on. A necessary condition for E_n to be minimal is the disappearance of all partial derivatives of E_n with respect to all α_j. We therefore calculate:

$$0 \overset{!}{=} \frac{\partial E_n}{\partial \alpha_j} = -\alpha_{j-1} + (2+K)\alpha_j - \alpha_n\delta_{nj} - \alpha_{j+1} + (L_0 - 1)\delta_{nj},\ j = 1\ldots n. \quad \text{(A14)}$$

This is a system of linear equations. Defining $\phi = 2+K$ we can write the augmented matrix of the system:

$$\left[\begin{array}{cccccc|c} \phi & -1 & 0 & \cdots & \cdots & 0 & 0 \\ -1 & \phi & -1 & & & \vdots & 0 \\ 0 & \ddots & \ddots & \ddots & & \vdots & \vdots \\ \vdots & & \ddots & \ddots & \ddots & 0 & \vdots \\ \vdots & & & -1 & \phi & -1 & 0 \\ 0 & \cdots & \cdots & 0 & -1 & \phi - 1 & 1 - L_0 \end{array}\right]. \quad \text{(A15)}$$

We solve the system via Gaussian elimination and defining:

$$m_i = \phi m_{i-1} - m_{i-2},\ m_0 = 1, m_1 = \phi, \quad \text{(A16)}$$

we get:

$$\alpha_i = (1 - L_0)\frac{m_{i-1}}{m_n - m_{n-1}},\ i = 1\ldots n. \quad \text{(A17)}$$

Eqn A16 is an order 2 linear homogeneous recurrence relation. It is solved by:

$$m_i = \frac{\lambda_1^{i+1} - \lambda_2^{i+1}}{\sqrt{\phi^2 - 4}}, \quad \text{(A18)}$$

$$\lambda_{1/2} = \frac{\phi}{2} \pm \sqrt{\frac{\phi^2}{4} - 1}. \quad \text{(A19)}$$

With Eqn A18 we can write Eqn A17 as a closed form expression for a_i only, depending on the ratio of the spring constants K and the number of segments n:

$$\alpha_i = (1 - L_0)\frac{\lambda_1^i - \lambda_2^i}{C_n}, \quad \text{(A20)}$$

where:

$$C_n = \sqrt{\phi^2 - 4}\left(m_n - m_{n-1}\right) = \left(\lambda_1^{n+1} - \lambda_1^n\right) - \left(\lambda_2^{n+1} - \lambda_2^n\right), \quad \text{(A21)}$$

which is a constant for a chain with n segments (Fig. 6E). For all $K>0$, this is a monotonically increasing function of segment index. Hence, the predicted chevron angles α_i always increase in the anteroposterior direction, independently of the free parameters K_a, K_x and L_0.

For stiff boundaries, $K_a \gg K_x$, hence $\phi \gg 2$ and therefore with Eqn A19:

$$\lambda_1 \approx \phi, \quad \text{(A22)}$$

$$\lambda_2 \approx 0, \quad \text{(A23)}$$

and thus the predicted chevron angles α_i grow exponentially with segment index for stiff boundaries:

$$\alpha_i \approx (1 - L_0)\phi^{i-n-1}. \quad \text{(A24)}$$

We definitely would not be able to experimentally detect chevron angles smaller than 1 deg. Hence, all segments would be detected as straight if all α_i<1 deg. With:

$$\alpha_i \approx (1 - L_0)\phi^{i-n-1} < \phi^{i-n-1} < \phi^{-1} = \frac{1}{2+K} \overset{!}{<} 1\,\text{deg} = 0.017\,\text{rad}, \quad \text{(A25)}$$

it follows that all segments appear straight for:

$$K > 60. \quad \text{(A26)}$$

Overdamped dynamics of the model

Assuming viscous damping, the overdamped equations of motion of our model system are:

$$\frac{\partial \alpha_i}{\partial t} = -\frac{1}{cL^2}\frac{\partial E_n}{\partial \alpha_i},\ i = 1\ldots n, \quad \text{(A27)}$$

where we introduced the viscous damping coefficient c. Using the earlier defined dimensionless energy (Eqn A10) and defining the dimensionless time,

$$\tilde{t} = t\frac{c}{K_x}, \quad \text{(A28)}$$

the dimensionless equations of motion read:

$$\frac{\partial \alpha_i}{\partial t} = -\frac{\partial E_n}{\partial \alpha_i} = -(2+K)\alpha_i + \alpha_{i-1} + \alpha_{i+1},\ i = 1\ldots n. \quad \text{(A29)}$$

As all segments are formed straight, the initial conditions read:

$$\alpha_i(t=0) = 0. \quad \text{(A30)}$$

A numerical solution of the equations of motion for seven segments is shown in Fig. 6F.

Acknowledgements

We are grateful to P. Brösamle and F. Schröder for help with image analysis, to O. Chara, A. Deutsch, T. Krüger, D. Richmond, J. Starruß and A. Voß-Böhme for fruitful discussions and to L. Bajard, P. Currie, S. Devoto, T. Lacalli, A. Webb and two anonymous reviewers for helpful comments on an earlier version of this manuscript.

Competing interests

The authors declare no competing financial interests.

Author contributions

F.R., A.C.O. and L.B. conceived this study. C.E. designed and carried out the experiments. F.R. and L.B. analysed the data and developed the model. F.R., A.C.O., L.B. and C.S. wrote the manuscript. All authors have read and approved the final manuscript.

Funding

This work was supported by the German Ministry for Education and Research [0315259 to F.R., L.B.]; the Max Planck Society [to C.E., C.S., A.C.O.]; the European Communities 7th Framework Programme [FP7/2007–2013, 207634 to C.S., A.C.O.]; the German Research Foundation [DFG OA21 to C.E.]; the Medical Research Council [MC_UP_1202/3 to A.C.O.]; and the Wellcome Trust [WT098025MA to A.C.O.]. Deposited in PMC for release after 6 months.

Supplementary material

Supplementary material available online at
http://jeb.biologists.org/lookup/suppl/doi:10.1242/jeb.102202/-/DC1

References

Agassiz, L. and Vogt, K. C. (1845). *Anatomie des Salmones*. Neuchâtel: Wolfrath.
Alexander, R. MN. (1969). The orientation of muscle fibres in the myomeres of fishes. *J. Mar. Biol. Assoc. UK* **49**, 263-290.

Barresi, M. J. F., D'Angelo, J. A., Hernández, L. P. and Devoto, S. H. (2001). Distinct mechanisms regulate slow-muscle development. *Curr. Biol.* **11**, 1432-1438.
Barrios, A., Poole, R. J., Durbin, L., Brennan, C., Holder, N. and Wilson, S. W. (2003). Eph/Ephrin signaling regulates the mesenchymal-to-epithelial transition of the paraxial mesoderm during somite morphogenesis. *Curr. Biol.* **13**, 1571-1582.
Bayly, M. B. (1974). An energy calculation concerning the roundness of folds. *Tectonophysics* **24**, 291-316.
Beattie, C. E. and Eisen, J. S. (1997). Notochord alters the permissiveness of myotome for pathfinding by an identified motoneuron in embryonic zebrafish. *Development* **124**, 713-720.
Bone, Q. and Moore, R. H. (2008). *Biology of Fishes*. New York, NY; Abingdon: Taylor & Francis.
Bordzilovskaya, N. P., Detlaff, T. A., Duhon, S. T. and Malacinski, G. M. (1989). Developmental-stage series of axolotl embryos. In *Developmental Biology of the Axolotl* (ed. J. B. Armstrong and G. M. Malacinski), pp. 201-219. New York, NY: Oxford University Press.
Chevrel, R. (1913). Essai sur la morphologie et la physiologie du muscle latéral chez les poissons osseux. *Arch. Zool. Exp. Gen.* **52**, 473-607.
Cortés, F., Daggett, D., Bryson-Richardson, R. J., Neyt, C., Maule, J., Gautier, P., Hollway, G. E., Keenan, D. and Currie, P. D. (2003). Cadherin-mediated differential cell adhesion controls slow muscle cell migration in the developing zebrafish myotome. *Dev. Cell* **5**, 865-876.
Currie, P. D. and Ingham, P. W. (1996). Induction of a specific muscle cell type by a hedgehog-like protein in zebrafish. *Nature* **382**, 452-455.
Daggett, D. F., Domingo, C. R., Currie, P. D. and Amacher, S. L. (2007). Control of morphogenetic cell movements in the early zebrafish myotome. *Dev. Biol.* **309**, 169-179.
Delsuc, F., Brinkmann, H., Chourrout, D. and Philippe, H. (2006). Tunicates and not cephalochordates are the closest living relatives of vertebrates. *Nature* **439**, 965-968.
Dent, J. N. (1956). Observations on the life history and development of *Leptodactylus albilabris*. *Copeia* **1956**, 207-210.
Devoto, S. H., Melançon, E., Eisen, J. S. and Westerfield, M. (1996). Identification of separate slow and fast muscle precursor cells in vivo, prior to somite formation. *Development* **122**, 3371-3380.
Dolez, M., Nicolas, J.-F. and Hirsinger, E. (2011). Laminins, via heparan sulfate proteoglycans, participate in zebrafish myotome morphogenesis by modulating the pattern of Bmp responsiveness. *Development* **138**, 97-106.
Du, S. J., Devoto, S. H., Westerfield, M. and Moon, R. T. (1997). Positive and negative regulation of muscle cell identity by members of the hedgehog and TGF-β gene families. *J. Cell Biol.* **139**, 145-156.
Durbin, L., Sordino, P., Barrios, A., Gering, M., Thisse, C., Thisse, B., Brennan, C., Green, A., Wilson, S. and Holder, N. (2000). Anteroposterior patterning is required within segments for somite boundary formation in developing zebrafish. *Development* **127**, 1703-1713.
Fan, C. M. and Tessier-Lavigne, M. (1994). Patterning of mammalian somites by surface ectoderm and notochord: evidence for sclerotome induction by a hedgehog homolog. *Cell* **79**, 1175-1186.
Feng, X., Adiarte, E. G. and Devoto, S. H. (2006). Hedgehog acts directly on the zebrafish dermomyotome to promote myogenic differentiation. *Dev. Biol.* **300**, 736-746.
Francis, E. T. B. (1934). *The Anatomy of the Salamander*. Oxford: Oxford University Press.
Gegenbaur, C. (1859). *Grundzüge der Vergleichenden Anatomie*. Leipzig: Wilhelm Engelmann.
Gray, R. S., Bayly, R. D., Green, S. A., Agarwala, S., Lowe, C. J. and Wallingford, J. B. (2009). Diversification of the expression patterns and developmental functions of the dishevelled gene family during chordate evolution. *Dev. Dyn.* **238**, 2044-2057.
Greene, C. W. and Greene, C. H. (1913). The skeletal musculature of the king salmon. *Bulletin of the US Bureau of Fisheries* **10**, 88-104.
Halpern, M. E., Ho, R. K., Walker, C. and Kimmel, C. B. (1993). Induction of muscle pioneers and floor plate is distinguished by the zebrafish no tail mutation. *Cell* **75**, 99-111.
Hammerschmidt, M., Bitgood, M. J. and McMahon, A. P. (1996). Protein kinase A is a common negative regulator of Hedgehog signaling in the vertebrate embryo. *Genes Dev.* **10**, 647-658.
Harder, W. (1964). *Anatomie der Fische, Textteil (Handbuch der Binnenfischerei Mitteleuropas – Bd. 2,A)*. Stuttgart: Schweizerbart.
Harrison, R. G. (1898). The growth and regeneration of the tail of the frog larva. *Archiv für Entwicklungsmechanik der Organismen* **7**, 430-485.
Hatschek, B. (1882). Studien über die Entwicklung des Amphioxus. *Arb. Aus Dem Zool. Instituten Univ. Wien Zool. Stn. Triest* **4**, 1-88.
Hatschek, B. (1893). *The Amphioxus and its Development*. London: Swan, Sonnenschein & Co.
Hatta, K., Bremiller, R., Westerfield, M. and Kimmel, C. B. (1991). Diversity of expression of engrailed-like antigens in zebrafish. *Development* **112**, 821-832.
Henry, C. A. and Amacher, S. L. (2004). Zebrafish slow muscle cell migration induces a wave of fast muscle morphogenesis. *Dev. Cell* **7**, 917-923.
Henry, C. A., McNulty, I. M., Durst, W. A., Munchel, S. E. and Amacher, S. L. (2005). Interactions between muscle fibers and segment boundaries in zebrafish. *Dev. Biol.* **287**, 346-360.
Herrgen, L., Schröter, C., Bajard, L. and Oates, A. C. (2009). Multiple embryo time-lapse imaging of zebrafish development. In *Zebrafish* (ed. G. J. Lieschke, A. C. Oates and K. Kawakami), pp. 243-254. New York, NY: Humana Press.
Hoar, W. S., Randall, D. J. and Conte, F. P. (1969). *Fish Physiology*. New York, NY: Academic Press.
Holley, S. A., Geisler, R. and Nüsslein-Volhard, C. (2000). Control of her1 expression during zebrafish somitogenesis by a delta-dependent oscillator and an independent wave-front activity. *Genes Dev.* **14**, 1678-1690.
Honjo, Y. and Eisen, J. S. (2005). Slow muscle regulates the pattern of trunk neural crest migration in zebrafish. *Development* **132**, 4461-4470.
Johnston, I. A., Bower, N. I. and MacQueen, D. J. (2011). Growth and the regulation of myotomal muscle mass in teleost fish. *J. Exp. Biol.* **214**, 1617-1628.
Kaestner, S. (1892). Über die allgemeine Entwicklung der Rumpf- und Schwanzmuskulatur bei Wirbeltieren. Mit bes. Berücksichtigung der Selachier. *Arch. Anat. Physiol. Anat. Abtlg*, 153-222.
Kimmel, C. B., Ballard, W. W., Kimmel, S. R., Ullmann, B. and Schilling, T. F. (1995). Stages of embryonic development of the zebrafish. *Dev. Dyn.* **203**, 253-310.
Koumans, J. T. M. and Akster, H. A. (1995). Myogenic cells in development and growth of fish. *Comp. Biochem. Physiol.* **110A**, 3-20.
Laale, H. W. (1982). Fish embryo culture: observations on axial cord differentiation in presomitic isolates of the zebrafish Brachydanio rerio (Hamilton-Buchanan). *Can. J. Zool.* **60**, 1710-1721.
Lacalli, T. (2012). The Middle Cambrian fossil Pikaia and the evolution of chordate swimming. *EvoDevo* **3**, 12.
Langelaan, J. W. (1904). On the form of the Trunk-myotome. In *Koninklijke Nederlandsche Akademie van Wetenschappen Proceedings* **7**, 34-40.
Lee, S. J., Kim, S., Choi, S.-C. and Han, J.-K. (2010). XPteg (*Xenopus* proximal tubules-expressed gene) is essential for pronephric mesoderm specification and tubulogenesis. *Mech. Dev.* **127**, 49-61.
Mallatt, J. and Holland, N. (2013). *Pikaia gracilens* Walcott: stem chordate, or already specialized in the Cambrian? *J. Exp. Zool. B* **320**, 247-271.
Maurer, F. (1913). Die ventrale Rumpfmuskulatur der Fische (Selachier, Ganoiden, Teleostier, Crossopterygier, Dipnoer). *Jena Z. Naturwiss.* **49**, 1-118.
Mchedlishvili, L., Epperlein, H. H., Telzerow, A. and Tanaka, E. M. (2007). A clonal analysis of neural progenitors during axolotl spinal cord regeneration reveals evidence for both spatially restricted and multipotent progenitors. *Development* **134**, 2083-2093.
Meyers, J. R., Planamento, J., Ebrom, P., Krulewitz, N., Wade, E. and Pownall, M. E. (2013). Sulf1 modulates BMP signaling and is required for somite morphogenesis and development of the horizontal myoseptum. *Dev. Biol.* **378**, 107-121.
Morin-Kensicki, E. M., Melancon, E. and Eisen, J. S. (2002). Segmental relationship between somites and vertebral column in zebrafish. *Development* **129**, 3851-3860.
Morris, S. C. and Caron, J.-B. (2012). *Pikaia gracilens* Walcott, a stem-group chordate from the Middle Cambrian of British Columbia. *Biol. Rev. Camb. Philos. Soc.* **87**, 480-512.
Müller, J. (1836). Vergleichende Anatomie der Myxinoiden, der Cyclostomen mit durchbohrtem Gaumen. Erster Theil. Osteologie und Myologie. *Abh. Königl. Akad. Wiss., Berlin* **1834**, 65-340.
Nursall, J. R. (1956). The lateral musculature and the swimming of fish. *Proc. Zool. Soc. Lond.* **126**, 127-144.
Oates, A. C. and Ho, R. K. (2002). Hairy/E(spl)-related (Her) genes are central components of the segmentation oscillator and display redundancy with the Delta/Notch signaling pathway in the formation of anterior segmental boundaries in the zebrafish. *Development* **129**, 2929-2946.
Press, W. H. (1996). *Numerical Recipes in C*. Cambridge: Cambridge University Press.
Prince, V. E., Joly, L., Ekker, M. and Ho, R. K. (1998). Zebrafish hox genes: genomic organization and modified colinear expression patterns in the trunk. *Development* **125**, 407-420.
Rauther, M. (1940). *Echte Fische (Dr. H.G. Bronns Klassen und Ordnungen des Tierreichs: 6. Bd., 1. Abt., 2. Buch)*. Leipzig: Akademische Verlagsgesellschaft.
Read, D. J., Duckett, R. A., Sweeney, J. and McLeish, T. C. B. (1999). Chevron folding instability in thermoplastic elastomers and other layered materials. *J. Phys. D Appl. Phys.* **32**, 2087-2099.
Riedel-Kruse, I. H., Müller, C. and Oates, A. C. (2007). Synchrony dynamics during initiation, failure, and rescue of the segmentation clock. *Science* **317**, 1911-1915.
Schindelin, J., Arganda-Carreras, I., Frise, E., Kaynig, V., Longair, M., Pietzsch, T., Preibisch, S., Rueden, C., Saalfeld, S., Schmid, B. et al. (2012). Fiji: an open-source platform for biological-image analysis. *Nat. Methods* **9**, 676-682.
Schröter, C., Herrgen, L., Cardona, A., Brouhard, G. J., Feldman, B. and Oates, A. C. (2008). Dynamics of zebrafish somitogenesis. *Dev. Dyn.* **237**, 545-553.
Schröter, C., Ares, S., Morelli, L. G., Isakova, A., Hens, K., Soroldoni, D., Gajewski, M., Jülicher, F., Maerkl, S. J., Deplancke, B. et al. (2012). Topology and dynamics of the zebrafish segmentation clock core circuit. *PLoS Biol.* **10**, e1001364.
Sepich, D. S., Ho, R. K. and Westerfield, M. (1994). Autonomous expression of the nic1 acetylcholine receptor mutation in zebrafish muscle cells. *Dev. Biol.* **161**, 84-90.
Sepich, D. S., Wegner, J., O'Shea, S. and Westerfield, M. (1998). An altered intron inhibits synthesis of the acetylcholine receptor α-subunit in the paralyzed zebrafish mutant nic1. *Genetics* **148**, 361-372.
Shann, E. W. (1914). On the nature of the lateral muscle in teleostei. *Proc. Zool. Soc. Lond.* **84**, 319-337.
Shu, D.-G., Morris, S. C. and Zhang, X.-L. (1996). A Pikaia-like chordate from the Lower Cambrian of China. *Nature* **384**, 157-158.
Singer, S. J. (1993). Layer buckling in smectic-A liquid crystals and two-dimensional stripe phases. *Phys. Rev. E Stat. Phys. Plasmas Fluids Relat. Interdiscip. Topics* **48**, 2796-2804.
Stickney, H. L., Barresi, M. J. F. and Devoto, S. H. (2000). Somite development in zebrafish. *Dev. Dyn.* **219**, 287-303.
te Kronnié, G. (2000). Axial muscle development in fish. *Basic Appl. Myol.* **10**, 261-267.

Turner, J. S. (2007). *The Tinkerer's Accomplice: How Design Emerges from Life Itself*. Cambridge, MA: Harvard University Press.
van der Meulen, T., Schipper, H., van Leeuwen, J. L. and Kranenbarg, S. (2005). Effects of decreased muscle activity on developing axial musculature in nicb107 mutant zebrafish (*Danio rerio*). *J. Exp. Biol.* **208**, 3675-3687.
van der Stelt, A. (1968). *Spiermechanica en Myotoombouw bij Vissen*. PhD dissertation University of Amsterdam, The Netherlands.
van Eeden, F. J. M., Granato, M., Schach, U., Brand, M., Furutani-Seiki, M., Haffter, P., Hammerschmidt, M., Heisenberg, C.-P., Jiang, Y.-J., Kane, D. A. et al. (1996). Mutations affecting somite formation and patterning in the zebrafish, *Danio rerio*. *Development* **123**, 153-164.
van Leeuwen, J. L. (1999). A mechanical analysis of myomere shape in fish. *J. Exp. Biol.* **202**, 3405-3414.
van Leeuwen, J. L., van der Meulen, T., Schipper, H. and Kranenbarg, S. (2008). A functional analysis of myotomal muscle-fibre reorientation in developing zebrafish *Danio rerio*. *J. Exp. Biol.* **211**, 1289-1304.
van Raamsdonk, W., van der Stelt, A., Diegenbach, P. C., van de Berg, W., Bruyn, H., van Dijk, J. and Mijzen, P. (1974a). Differentiation of the musculature of the teleost Brachydanio rerio. I. Myotome shape and movements in the embryo. *Anat. Embryol. (Berl)* **145**, 321-342.
van Raamsdonk, W., van Der Stelt, A., Diegenbach, P. C. and Nijzen, P. (1974b). Nederlandse dierkundige vereniging (Netherlands Zoological Society). *Neth. J. Zool.* **25**, 376.
van Raamsdonk, W., Pool, C. W., Mijzen, P., Mos, W. and van der Stelt, A. (1977). On the relation between movements and the shape of the somites in early embryos of the teleost *Brachydanio rerio*. *Bijdr. Tot Dierkd.* **46**, 261-274.
van Raamsdonk, W., Pool, C. W. and te Kronnie, G. (1978). Differentiation of muscle fiber types in the teleost *Brachydanio rerio*. *Anat. Embryol. (Berl.)* **153**, 137-155.
van Raamsdonk, W., Mos, W., Tekronnié, G., Pool, C. W. and Mijzen, P. (1979). Differentiation of the musculature of the teleost *Brachydanio rerio*. II. Effects of immobilization on the shape and structure of somites. *Acta Morphol. Neerl. Scand.* **17**, 259-273.
Videler, J. J. (1993). *Fish Swimming*. Suffolk: Chapman & Hall.
von Seckendorff Hoff, K. and Wassersug, R. J. (1986). The kinematics of swimming in larvae of the clawed frog, *Xenopus laevis*. *J. Exp. Biol.* **122**, 1-12.
Weinberg, E. S., Allende, M. L., Kelly, C. S., Abdelhamid, A., Murakami, T., Andermann, P., Doerre, O. G., Grunwald, D. J. and Riggleman, B. (1996). Developmental regulation of zebrafish MyoD in wild-type, no tail and spadetail embryos. *Development* **122**, 271-280.
Westerfield, M., Liu, D. W., Kimmel, C. B. and Walker, C. (1990). Pathfinding and synapse formation in a zebrafish mutant lacking functional acetylcholine receptors. *Neuron* **4**, 867-874.
Wickström, A. (1897). Über die Innervation und den Bau der Myomeren der Rumpfmuskulatur einiger Fische. *Anat. Anz.* **13**, 401-408.
Willemse, J. J. (1966). Functional anatomy of the myosepta in fishes. *Proc. K. Ned. Akad. Wet. C.* **69**, 58-63.
Windner, S. E., Bird, N. C., Patterson, S. E., Doris, R. A. and Devoto, S. H. (2012). Fss/Tbx6 is required for central dermomyotome cell fate in zebrafish. *Biol. Open* **1**, 806-814.
Wolff, C., Roy, S. and Ingham, P. W. (2003). Multiple muscle cell identities induced by distinct levels and timing of hedgehog activity in the zebrafish embryo. *Curr. Biol.* **13**, 1169-1181.
Wunder, W. (1936). *Physiologie der Süßwasserfische Mitteleuropas (Handbuch der Binnenfischerei Mitteleuropas – Bd. 2,B)*. Stuttgart: Schweizerbart.
Yin, C. and Solnica-Krezel, L. (2007). Convergence and extension movements affect dynamic notochord-somite interactions essential for zebrafish slow muscle morphogenesis. *Dev. Dyn.* **236**, 2742-2756.
Yoshigai, E., Kawamura, S., Kuhara, S. and Tashiro, K. (2009). Trim36/Haprin plays a critical role in the arrangement of somites during *Xenopus* embryogenesis. *Biochem. Biophys. Res. Commun.* **378**, 428-432.

The Journal of Experimental Biology

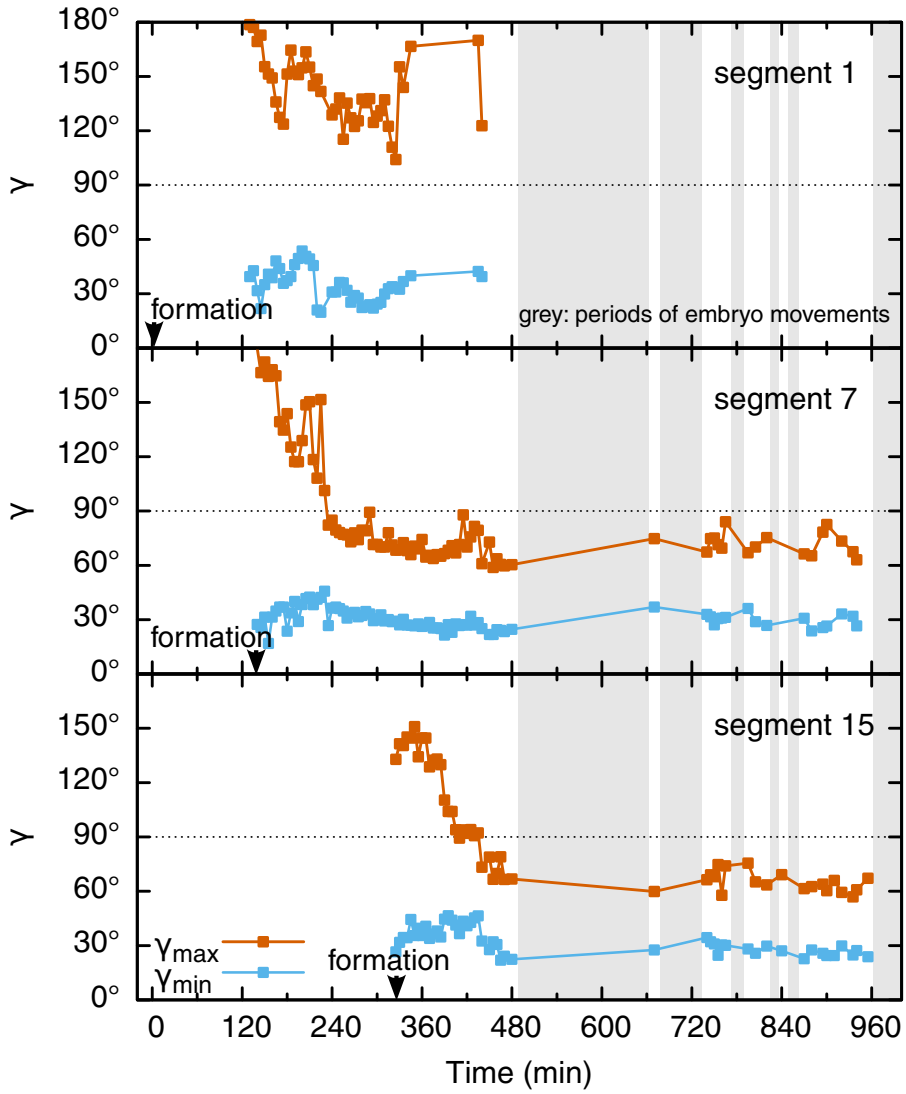

Fig. S1. Raw angle data, γ_{min} and γ_{max}, used to calculate $\alpha \pm \Delta\alpha$ for Fig. 2C–E.

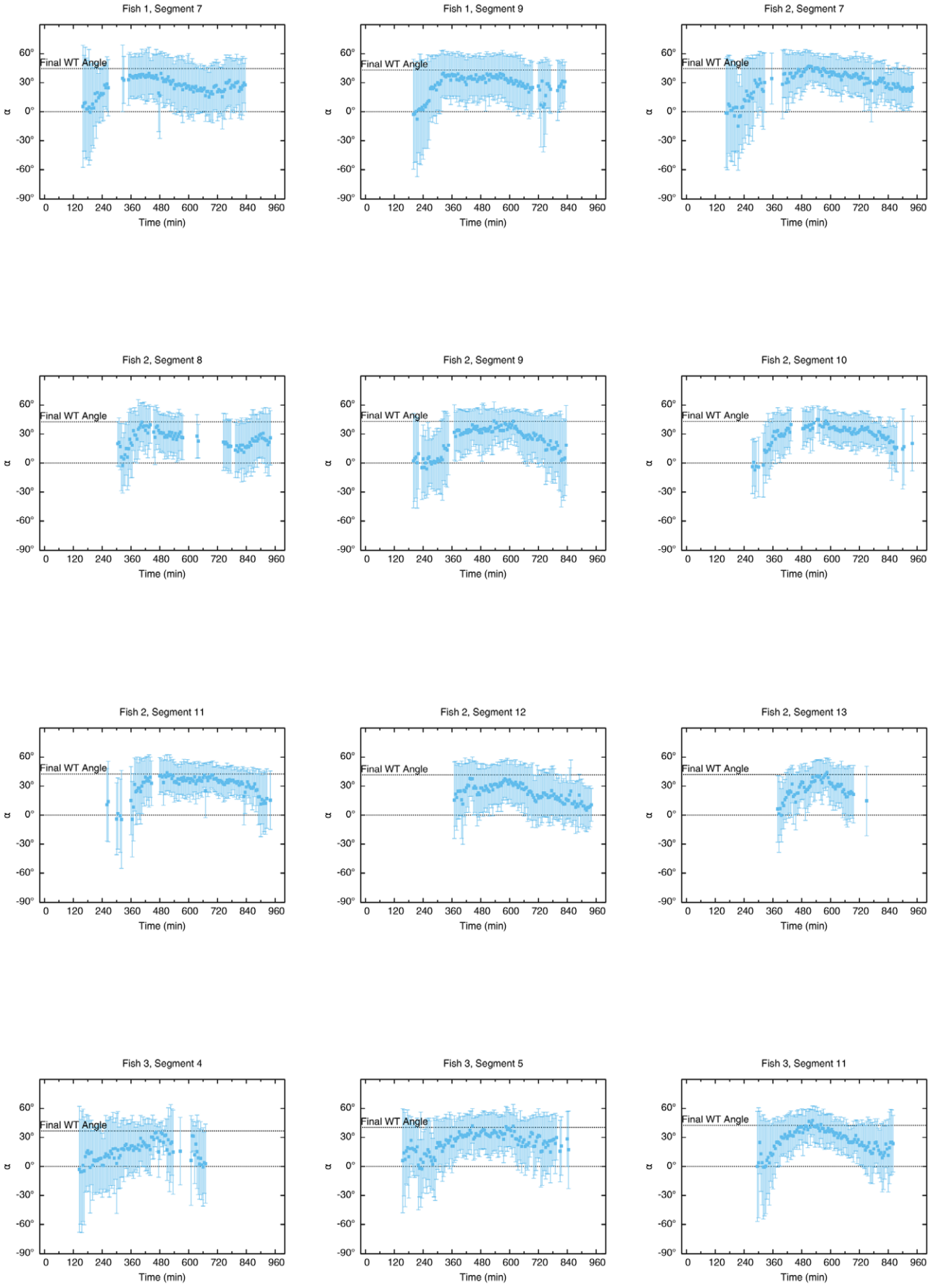

Fig. S2. Multiple time series of chevron angle, α, of embryos treated with cyclopamine. For all these segments, chevrons formed with normal angle but then relaxed. Fish 2, segment 7 is also shown in Fig. 2H.

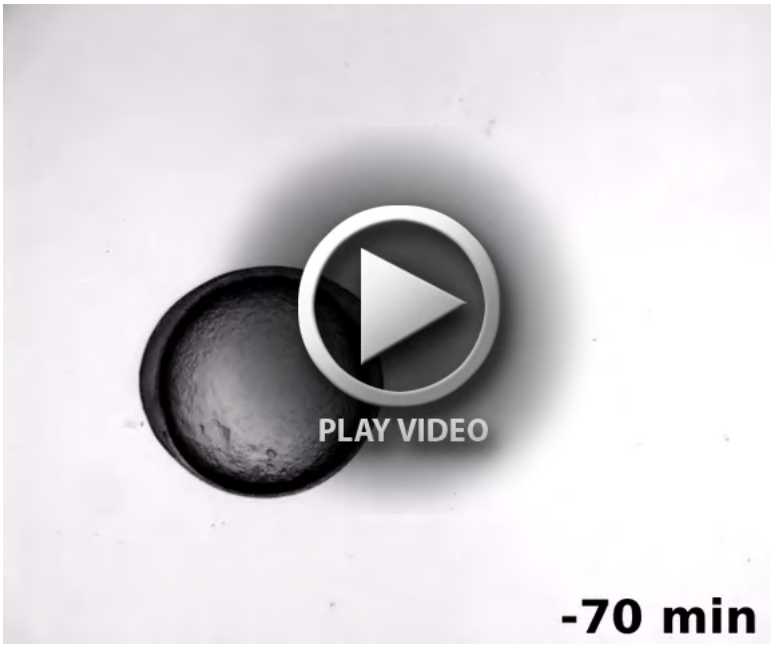

Movie 1. Developing mobile zebrafish (Figs 1, 2). First movements start at 480 min, when 17 segments have formed. However, movements are burst-like and for a number of frames, angle measurements remain possible.

Movie 2. Developing immobile zebrafish (homozygous *nic*^{b107} mutant). From about 400 min on the vacuolating cells of the notochord become visible. They clearly move posteriorly relative to the segment boundaries. At this time the segments are already chevron shaped.

Movie 3. Developing zebrafish treated with cyclopamine. Raw angle data OpenDocument Spreadsheet file containing all original measurements of chevron angles γ_{min} and γ_{max} (Figs 2A,B, 4H; supplementary material Figs S1, S2).

Table S1. Chevron formation of the zebrafish muscle segments

Download Table S1